BB

ISSN 1346-244X
RIKEN-AF-NP-424

Measurements of the Interaction Cross Sections for Ar and Cl isotopes

A. Ozawa, T. Baumann, L. Chulkov, D. Cortina, U. Datta, J. Fernandez, H. Geissel, F. Hammache, K. Itahashi, M. Ivanov, R. Janik, T. Kato, K. Kimura, T. Kobayashi, K. Markenroth, M. Meister, G. Münzenberg, T. Ohtsubo, S. Ohya, T. Okuda, A. A. Ogloblin, V. Pribora, M. Sekiguchi, B. Sitár, P. Strmen, S. Sugimoto, K. Sümmerer, T. Suzuki, I. Tanihata, and Y. Yamaguchi

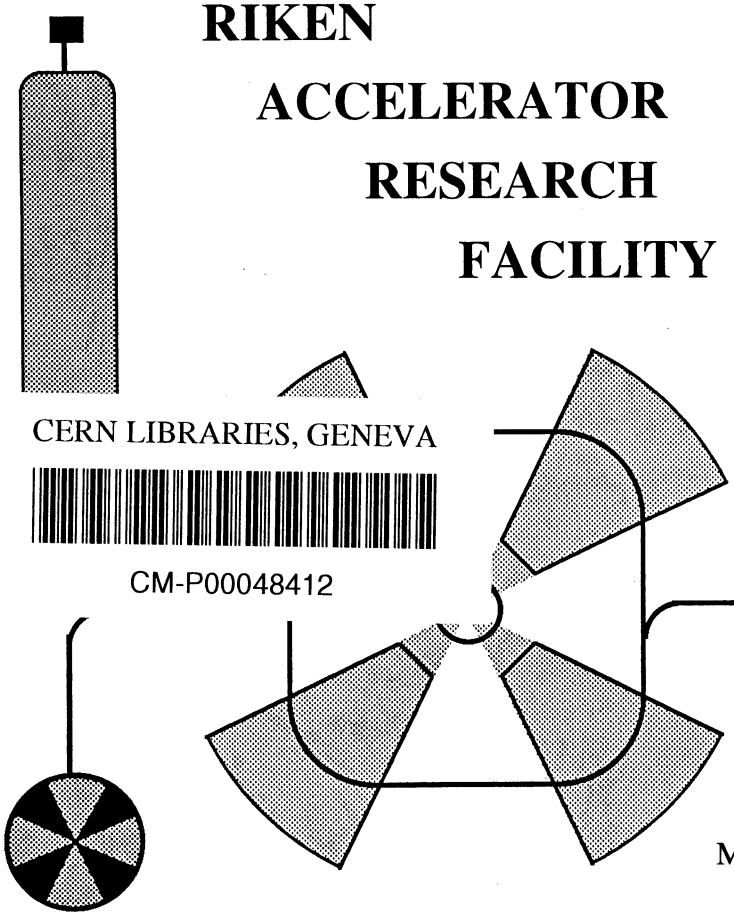

May 2002

The Institute of Physical and Chemical Research (RIKEN)
2-1 Hirosawa, Wako, Saitama 351-0198, Japan
TEL: (048)462-1111 FAX: (048)462-4642
e-mail: *username*@rikvax.riken.go.jp

Measurements of the Interaction Cross Sections for Ar and Cl isotopes

A.Ozawa[1], T.Baumann[2], L.Chulkov[4], D.Cortina[7], U.Datta[2], J.Fernandez[7], H.Geissel[2], F.Hammache[2], K.Itahashi[1], M.Ivanov[5], R.Janik[5], T.Kato[3], K.Kimura[9], T.Kobayashi[8], K.Markenroth[6], M.Meister[6], G.Münzenberg[2], T.Ohtsubo[3], S.Ohya[3], T.Okuda[8], A.A.Ogloblin[4], V.Pribora[4], M.Sekiguchi[8], B.Sitár[5], P.Strmen[5], S.Sugimoto[1], K.Sümmerer[2], T.Suzuki[3], I.Tanihata[1], Y.Yamaguchi[3]

[1]*The Institute of Physical and Chemical Research (RIKEN), Hirosawa 2-1, Wako-shi, Saitama 351-0198, Japan*

[2]*Gesellschaft für Schwerionenforschung (GSI), Planckstrasse 1, D-64291, Darmstadt, Germany*

[3] *Department of Physics, Niigata University, Niigata 950-2181, Japan*

[4]*Kurchatov Institute, Kurchatov sq. 1, 123182 Moscow, Russia*

[5]*Faculty of Mathematics and Physics, Comenius University, 84215 Bratislava, Slovak Republic*

[6] *Department of Experimental Physics, Chalmers University of Technology, SE-412 96 Göteborg, Sweden*

[7] *Department of Physics, University of Santiago Compostela, E-15706 Santiago de Compostela, Spain*

[8] *Department of Physics, Tohoku University, Miyagi 980-8578, Japan*

[9]*Nagasaki Institute of Applied Science, Nagasaki-shi, Nagasaki 851-01, Japan*

Abstract

We have measured the interaction cross-sections (σ_I) of $^{31-40}$Ar and $^{31-37}$Cl on carbon targets at energies of around 950*A* MeV. The effective matter radii for these nuclei were deduced by a Glauber-model analysis. Combining our matter radii with measured proton radii for Ar isotopes, we could deduce the proton-skin thicknesses for the $^{32-40}$Ar isotopes, which were found to increase monotonically with decreasing neutron number. The larger radius of the proton drip-line nucleus ^{31}Ar suggests an anomalous structure for this nucleus. In addition, using NaI(Tl) arrays surrounding the carbon target, we measured γ-rays emitted from excited states in these isotopes. In this way we could deduce the upper limits for the inelastic cross-sections (σ_{inela}) on carbon targets at energies of around 950*A* MeV.

PACS numbers: 21.10.Gv, 25.60.Dz, 27.30.+t, 27.40.+z

Keywords: NUCLEAR REACTIONS C($^{31-40}$Ar, $^{31-40}$Ar); C($^{31-37}$Cl, $^{31-37}$Cl); E ~ 950 MeV/nucleon; measured interaction σ; measured in-elastic σ; $^{31-40}$Ar and $^{31-37}$Cl deduced effective radii; proton skins for $^{32-40}$Ar

1. Introduction

The interaction cross-sections (σ_I) and reaction cross-sections (σ_R) for light nuclei have been extensively studied at many radioactive nuclear beam facilities (see, e.g., [1]). In particular, at relativistic energies, these measurements provide a method to determine effective matter radii and effective matter densities as well as information about the valence nucleons of unstable nuclei [1]. While our previous studies with this method [2,3,4,5] were limited to Z = 12, the present study was aimed at investigating if the method can also be applied to heavier nuclei.

One of the most interesting features of unstable nuclei is the existence of skins. Evidence for neutron skins in unstable nuclei has been collected for ^{6}He and ^{8}He for the first time [6]. Measurements of Na isotopes [2,3] have revealed a monotonic increase in the neutron skin thickenesses with increasing neutron number. Some nuclear theories, for example Relativistic Mean Field (RMF) theory [7] and a Hartree-Fock model with a Skyrme interaction [8], reproduce the neutron skins well. Such models also predict the existence of proton skins in proton-rich nuclei. However, no clear experimental evidence has been obtained so far. For ^{20}Mg, an isotope located at proton-drip line, a thick proton skin is suggested from the difference of σ_I between ^{20}Mg and its mirror partner, ^{20}O [4]. However, quantitative conclusions cannot be drawn, since the proton radius is not known for ^{20}Mg. In contrast, argon isotopes can provide quantitative information on proton-skins, since their proton radii of $^{32\text{-}40}$Ar have been studied by optical isotope shift measurements [9].

To derive effective matter radii from measured σ_I, we perform a Galuber model analysis. In this context it is important to distinguish between the "reaction" and "interaction" cross sections. By definition, $\sigma_R = \sigma_I + \sigma_{inela}$, where σ_{inela} is the inelastic cross section. Glauber-model calculations show that the difference between σ_I and σ_R at relativistic energies (around 900 A MeV) is only a few %, which is very close to the experimental error bars of σ_I [10]. Therefore, we always assume $\sigma_I \approx \sigma_R$ for an analysis at relativistic energies. However, until now, we have no experimental evidence for this assumption. The present experiment used an NaI(Tl) array to detect γ-rays emitted from the projectile, and thus allowed us to estimate σ_{inela} of the projectile.

In this paper, our experimental setup and results are described in Section 2. We also describe measurements of σ_{inela}. A discussion of σ_I is given in Section 3. In Section 4, the deduced matter radii and proton skins are described. We present our conclusions in Section 5.

2. Experimental procedure and results

The experiment was performed at the projectile-FRagment Separator (FRS) [11] at GSI. Secondary beams of $^{31\text{-}35}$Ar ($^{36\text{-}39}$Ar) and $^{31\text{-}33}$Cl ($^{34\text{-}37}$Cl) were produced via the projectile fragmentation of a ^{36}Ar (^{40}Ar) primary beam accelerated to around 1A GeV by the heavy-ion synchrotron SIS. A total of 11 different settings of the FRS were used to separate and transmit $^{31\text{-}40}$Ar as nominal fragments. The fragments under study were separated in the first half of the FRS, with selection made only according to their mass-over-charge ratios. This allowed us to also determine σ_I for Cl isotopes together with those for the Ar isotopes selected by the FRS setting, as shown in Table 1. The primary-beam energies and the thicknesses of the Be production targets were adjusted isotope by isotope so that the energies per nucleon of the secondary beams at the middle of the reaction targets would be around 950A MeV, as listed in Table 1. The maximum primary beam intensities of 2×10^9 particles per spill were used to produce nuclei near to the proton drip-line. The typical spill lengths were 4 sec. We note that the purity of secondary beams is worse on the proton-rich side. For ^{31}Ar, the purity was roughly 1×10^{-4}.

Figure 1 shows a schematic drawing of the experimental setup. The experimental setup was essentially the same as that for our previous measurements [5]. At the first focus (F1), we placed a scintillation counter (thickness t = 3 mm) to obtain the start signal for a time-of-flight (TOF) measurement. This detector was also used as an active slit for momentum definition ($\Delta p/p$ = ±0.25%). At the intermediate focus (F2) of FRS (dispersion = 4.4 cm/%), we installed a scintillation counter as the timing counter (width w = 120 mm and t = 3 mm; flight path length s = 17.8 m), and four Time-Projection Chambers (TPC), which were developed at Comenius University in Slovakia [12]. In order to measure the energy-loss of fragments, we installed an Ionization Chamber (IC) capable of accepting high count rates, which were developed in Münich [13]. The IC provides four anode pulse-height data (A_i). The geometric average of the four pulse-height data in the IC corresponds to ΔE of the beam at F2. From the TOF scintillation counters we also obtained the horizontal position at the foci. Thus, the position information at foci F1 and F2 together with the magnetic field in the second dipole gave $B\rho$ of the fragments. This allowed us to calculate A and Z from $B\rho$, TOF, and ΔE, providing particle identification up to F2.

Reaction targets of carbon with 2.755 g/cm^2, 4.405 g/cm^2 and 5.356 g/cm^2 thickness were placed at F2. The uniformity of the target thicknesses was better than ±0.06%. At the final achromatic focus (F4) of FRS, we placed two TPC, a MUlti-Sampling Ion-

Chamber (MUSIC) and a scintillation counter (w = 200 mm and t = 5 mm). The plastic detector at F2 served as a start signal for TOF and the scintillator at F4 as a stop signal (s = 36.9 m). MUSIC provided four anode pulse-height data. The geometric average of the four pulse-height signals corresponds to ΔE of the beam at F4. ΔE was calibrated using the primary beam (Z = 18) at the beginning of the experiment. The scintillation counter at F4 also provided the horizontal position at this focus. Thus, position information at foci F2 and F4 together with the magnetic fields in the third and fourth dipoles gave $B\rho$ of the fragments. This allowed us to determine A and Z from $B\rho$, TOF, and ΔE behind the reaction targets. A typical particle-identification spectrum for ^{33}Ar setting in the first and second half is shown in Fig. 2.

To measure σ_{inela}, γ-rays emitted in coincidence with secondary beams impinging on the reaction targets were observed in a NaI(Tl) array, which consisted of 32 NaI(Tl) crystals located approximately 80 cm behind the reaction target at F2, as shown in Fig. 1. The array had 3% of total efficiency, including geometry; its energy resolution ($\Delta E/E$) amounted to 12% (FWHM), for E_γ = 429 keV [14]. The four TPC at F2 could provide precise positions and emission angles of the beams before and after the reaction target, which allowed us to correct the Doppler shifts of the γ-rays emitted from the secondary beams.

The data-analysis method to obtain σ_I was the same as that in our previous experiments. σ_I were calculated using the equation $\sigma_I = (1/N_t) \ln(\Gamma_0/\Gamma)$, where Γ is the ratio of the number of non-interacting ions to that of the incoming ions for a target-in run, and Γ_0 is the same ratio for an empty-target run. The number of target nuclei per unit area is denoted by N_t. It is crucial for transmission measurements to accurately count all non-interacting ions downstream from the F2 reaction target. In order to secure full transmission for non-interacting nuclei in the second half of the FRS, we selected incident nuclei with a small angular divergence ($\leq \pm 9$ mrad) based on the position information of two TPC upstream from the reaction targets at F2.

In this experiment, we had to cope with widely varying count rates. The count rates at F1, F2 and F4 changed considerably from isotope to isotope, and also changed when measuring with or without reaction targets (200/spill to 600k/spill). On the other hand, in some detectors, the resolution became worse at a high count rate. For example, MUSIC at F4 gave a good energy resolution only for less than 10 k/spill. Thus, we observed a strong count-rate dependence for Γ_0 and Γ. We took the count-rate dependence into account to deduce σ_I, as follows. We measured Γ_0 and Γ with different targets for several runs, while monitoring the F4 count rates for each run. By using this empirical dependence, we normalized Γ_0 to the corresponding count rate of

the runs that gave Γ. After this procedure, we deduced σ_I for each run and took the average of the runs with the same targets. We found a consistency of the results from the thick and thin targets; thus, the final value was obtained by averaging them. The measured σ_I are listed in Table 2. As shown in Table 1, we measured σ_I for ^{36}Ar with two different settings: one was with the ^{36}Ar primary beam; the other one was as a fragment produced from the ^{40}Ar projectile. The results of the two settings are identical, as shown in Table 2. This consistency verifies the validity of the method.

We obtained the γ-ray spectra emitted by the secondary beams as they passed through the reaction targets. We did not observe any pronounced γ-ray peaks. In Fig. 3, we show as an example the γ-ray spectrum obtained for ^{34}Cl (selected at both F2 and F4) with a 5.356 g/cm^2 thick carbon reaction-target. Several excited states in ^{34}Cl are known, as shown in the inset in Fig. 3. From the level scheme, we simulated possible γ-ray spectra, while also taking also into account the efficiency, including the geometry and the energy resolution of the NaI(Tl) array. The total detection efficiency of the NaI(Tl) array was simulated using GEANT [15]. In addition to the peaks, we approximated the background by an exponential. In Fig. 3, different lines corresponding to different values of σ_{inela} are shown. We take the full line (calculated for σ_{inela} = 10 mb) as an upper limit. Thus, we conclude that, at relativistic energy, σ_{inela} is smaller than the typical errors of σ_I and, therefore, $\sigma_I \approx \sigma_R$. This corroborates with theoretical calculations [10], which arrived at similar conclusions.

3. Discussions of the interaction cross-sections

The measured σ_I are shown as a function of the mass number (A) for the Ar and Cl isotopes in Fig. 4. The observed σ_I increased monotonically with A. The solid lines in Fig. 4 show the σ_I values calculated using the equation

$$\sigma_I = \pi [R_I(^{12}C) + r_0 A^{1/3}]^2, \qquad (1)$$

where $R_I(^{12}C)$ is the interaction radius of ^{12}C (2.61 fm [1]) and r_0 is selected to reproduce σ_I of ^{36}Ar (^{37}Cl) for Ar (Cl) isotopes, respectively.

For both series of isotopes, the observed rate of increase is well reproduced by Eq. (1). The large σ_I of ^{31}Ar could indicate an extended proton distribution in this nucleus. One can see that the radii of $N = Z$ nuclei, ^{36}Ar and ^{34}Cl, are somewhat larger than those of their neighbors. In the light-mass region, a similar tendency could be observed [4,16]. There, the large radii were interpreted to be due to α-cluster formation [16] or, in the case of ^{20}Ne, to a deformation [4].

4. Matter radii and proton skins

4.1 Effective root-mean-square matter radii

Effective Root-Mean-Square (RMS) matter radii of the nucleon distributions were deduced from σ_I using the Glauber model in the optical-limit approximation (GMOL), the details of which are described in Ref. [1]. For lighter exotic nuclei, calculations of RMS matter radii have been developed by Ogawa *et al.* [10] and Al-Khalili *et al.* [17] using the Galuber model for few-body systems (GMFB). For those cases, GMFB calculations give larger RMS radii than GMOL, particularly for halo nuclei, such as ^{11}Be and ^{11}Li. The two approaches differ appreciably, however, only for loosely bound systems (neutron separation energies; S_n < 1 MeV) [5]. For nuclei with large separation energies, GMFB calculations give almost the same results as those by GMOL [5]. For the present case, the lowest proton separation energy (S_p) is 290±50 keV for ^{31}Cl [18]. However, the Coulomb barrier for the valence proton is roughly ~3 MeV for Z = 17. Thus, we conclude that the GMOL approach is fully sufficient to analyze the present data.

Glauber model calculations require that the functional form of the density distribution is specified. In the light-mass region, Harmonic-Oscillator (HO) type density distributions reproduce the densities well [1]. For the heavier mass system, a Fermi-type distribution reproduces the effective nucleon densities much better [1]. Numerically, the density is described as

$$\rho(r) = \rho_0 [\ 1 + \exp((r-R)/a)\ ]^{-1}, \qquad (2)$$

where R and a are the radius and the diffuseness parameters, respectively. Since we measure only one observable (σ_I), but need to determine two parameters (R and a), we have to fix either R or a. We have chosen to fix a to the value obtained for stable ^{36}Ar (a = 0.507 fm [19]) and vary the radius parameter (R) in Eq. (2). We showed previously for Na and Mg isotopes that consistent values of the deduced matter radii were obtained when changing either R or a; both approaches were able to reproduce the σ_I within their error bars [2,3].

By integrating the effective densities (Eq. (2)) we deduced the effective RMS matter radii. The results are listed in Table 3 and visualized in Fig. 5. In this figure we also show, by the solid lines, the results from RMF calculations with NL3 parameterization [20]. The RMF calculations generally predict larger radii, but reproduce the mass dependence of the experimental data well.

In Fig. 5, we can observe a larger radius of a proton drip-line nucleus ^{31}Ar. To investigate this in more detail, we show in Fig. 6 the isospin dependence of the RMS

matter radii for $A = 31$ isobars. Unfortunately, the radius of ^{31}Al, the mirror partner of ^{31}Ar, is not known, but data are available for more neutron-rich nuclei, ^{31}Mg and ^{31}Na [3]. Fig. 6 reveals the ^{31}Ar radius is indeed somewhat larger than that of ^{31}Mg and ^{31}Na. Thus, it is suggested that the mirror symmetry of the radii is breaking at ^{31}Ar. This kind of mirror asymmetry is also shown in ^{17}Ne [21] and ^{20}Mg [4]. A possible proton halo structure is suggested for ^{17}Ne [22], and the deformation effect would explain the asymmetry radii in ^{20}Mg [22]. Thus, a proton halo and/or a large deformation may be anticipated for ^{31}Ar.

4.2 Proton skins

In order to extract numerical values for the proton-skin thickness, we used the following equation for the matter radii:

$$(R_{rms}^{m})^2 = (Z/A)(R_{rms}^{p})^2 + (N/A)(R_{rms}^{n})^2, \qquad (3)$$

where R_{rms}^{m}, R_{rms}^{p} and R_{rms}^{n} are RMS matter, proton and neutron radii, respectively. To separate neutron and proton radii, we subtracted from our matter radii (Col. 2 of Table 3) the experimental RMS proton radii of the Ar isotopes obtained by optical isotope shifts measurements [9]. To obtain the values shown in Col. 3 of Table 3, we normalized the ^{36}Ar radius to the one determined by electron scattering [19]. Thus, we obtained the RMS neutron radii listed in Col. 4 of Table 3. The proton skin thickness is given by $(R_{rms}^{p} - R_{rms}^{n})$, as listed in Col. 5 of Table 3 and visualized in Fig. 7. The errors of the skin thicknesses were dominated by the errors of the RMS matter radii.

For a comparison, we also plot in Fig. 7 the proton skin thicknesses obtained by RMF calculations with the NL3 parameter set (the solid line). The RMF calculations reproduce the observed tendency very well. In the figure, the proton-skin thickness increases monotonically with decreasing mass number. While a similar constant increase of neutron skins with increasing neutron number has been observed for Na-isotopes [2], we can demonstrate for the first time a monotonical increase of proton skins. The two observations, together with good agreement with the RMF calculations, indicate that neutron as well as proton skins are quite common phenomena in unstable nuclei off the stability line.

Previously, we correlated the skin thickness with the difference between the proton and neutron separation energies, S_p-S_n [2]. A similar plot is shown in Fig. 8; it includes the neutron-skin thicknesses deduced previously for the Na-isotopes [2]. We can see a strong correlation of the skin thickness with S_p-S_n. Thus, it is shown that the difference between proton and neutron Fermi-energies in the nucleus is the driving force that creates the skin phenomenon. Such a correlation is also predicted by RMF

calculations [6]. In Fig. 8, results from the RMF calculations with NL3 are shown by the cross marks. At first glance, the present RMF calculations reproduce the experimental correlations well. However, in detail, the present RMF calculations fail to reproduce ^{37,38}Ar and predict smaller S_p-S_n for the Na isotopes. Improvements of calculations are anticipated.

5. Conclusion

In summary, we have measured the interaction cross-sections (σ_I) for $^{31\text{-}40}$Ar and $^{31\text{-}37}$Cl on carbon targets at relativistic energies. We also measured γ-rays emitted from the nuclei passing through the carbon targets to estimate the inelastic cross-sections (σ_{inela}). We did not observe any prominent γ-ray peaks for the nuclei, which implies that σ_{inela} should be less than about 10 mb. This number is the same size as typical errors of σ_I. Thus, our assumption that $\sigma_I \approx \sigma_R$ at relativistic energies seems to be justified.

We deduced the effective matter radii of the nuclei by a Glauber-model analysis. The deduced matter radius of ^{31}Ar is larger than those of its neighbors. This suggests an anomalous structure. We deduced the proton skin thicknesses of Ar isotopes by combining the deduced matter radii with proton radii obtained from optical isotope-shift measurements. The data show, for the first time, a monotonical increase of proton skins with decreasing neutron number. We also observed a strong correlation of the skin thickness with the difference of the proton and the neutron separation energies. That suggests that the Fermi-energy difference for protons and neutrons in the nucleus is essential for skin phenomena.

Acknowledgements

We would like to thank the members of the FRS group and SIS staff members for their help, in particular K.-H.Behr, A.Brünle and K.Burkard for their technical assistance. The first author (A.O.) acknowledges support from T.Suda.

References

[1] A.Ozawa *et al.*, Nucl. Phys. A **693**, 32 (2001).
[2] T.Suzuki *et al.*, Phys. Rev. Lett., **75** 3241 (1995).
[3] T.Suzuki *et al.*, Nucl. Phys. A **630**, 661 (1998).
[4] L.Chulkov *et al.*, Nucl. Phys. A **603**, 219 (1996).
[5] A.Ozawa *et al.*, Nucl. Phys. A **691**, 599 (2001).
[6] I.Tanihata *et al.*, Phys. Lett. B **289**, 261 (1992).
[7] Y.Sugahara *et al.*, Prog. Theor. Phys. **96**, 1165 (1996) and references therein.
[8] B.A.Brown and W.A.Richter, Phys. Rev. C **54**, 673 (1996).
[9] A.Klein *et al.*, Nucl. Phys. A **607**, 1 (1996).
[10] Y.Ogawa *et al.*, Nucl. Phys. A **543**, 722 (1992).
[11] H.Geissel *et al.*, Nucl. Instr. Meth. B **70**, 286 (1992).
[12] V.Hlinka *et al.*, Nucl. Instr. Meth. A **419**, 503 (1998).
[13] A.Stolz *et al.*, GSI Scientific Report 1998, p.174 (1999).
[14] D.Cortina-Gil *et al.*, Phys. Lett. B **529**, 36 (2002).
[15] J.Apostolakis, http://wwwinfo.cern.ch/asd/geant/index.html (2000).
[16] A.Ozawa *et al.*, Nucl. Phys. A **608**, 63 (1996) and references therein.
[17] J.S.Al-Khalili and J.A.Tostevin, Phys. Rev. Lett. **76**, 3903 (1996).
[18] G.Audi and A.H.Wapstra, Nucl. Phys. A **595**, 409 (1995).
[19] H.De Vries *et al.*, At. Data Nucl. Data Tables **36**, 495 (1987).
[20] G.A.Lalazissis *et al.*, Phys. Rev. C **55**, 540 (1997).
[21] A.Ozawa *et al.*, Phys. Lett. B **334**, 18 (1994).
[22] H.Kitagawa, N.Tajima,H.Sagawa, Z. Phys. A **358**, 381 (1997).

Table 1

Primary beam energies and Be target thicknesses used in each setting. The nominal fragments of the individual settings are underlined.

Primary beam	Fragments	Primary beam energy (A MeV)	Be target thickness (mg/cm^2)
^{40}Ar	-	1035	2512
^{40}Ar	$\underline{^{39}\text{Ar}}$, ^{37}Cl	1035	1625
^{40}Ar	$\underline{^{38}\text{Ar}}$, ^{36}Cl	1035	1625
^{40}Ar	$\underline{^{37}\text{Ar}}$, ^{35}Cl	1035	1625
^{40}Ar	$\underline{^{36}\text{Ar}}$, ^{34}Cl	1035	1625
^{36}Ar	-	1050	2512
^{36}Ar	$\underline{^{35}\text{Ar}}$, ^{33}Cl	1050	1625
^{36}Ar	$\underline{^{34}\text{Ar}}$, ^{32}Cl	1050	1625
^{36}Ar	$\underline{^{33}\text{Ar}}$, ^{31}Cl	1050	1625
^{36}Ar	$\underline{^{32}\text{Ar}}$	1050	1625
^{36}Ar	$\underline{^{31}\text{Ar}}$	1050	1625

Table 2

Interaction cross sections (σ_I) for Ar and Cl isotopes with carbon targets.

Nucleus	Mean energy/A	σ_I
	(MeV)	(mb)
^{31}Ar	940	1358±34
^{32}Ar	940	1317±33
^{33}Ar	950	1330±32
^{34}Ar	950	1356±14
^{35}Ar	955	1369±15
^{36}Ar*	945	1386±14
^{36}Ar**	940	1386±23
^{37}Ar	945	1378±15
^{38}Ar	950	1398±14
^{39}Ar	950	1434±14
^{40}Ar	940	1452±14
^{31}Cl	960	1288±52
^{32}Cl	960	1306±56
^{33}Cl	960	1289±34
^{34}Cl	945	1334±28
^{35}Cl	945	1327±14
^{36}Cl	945	1365±14
^{37}Cl	945	1374±14

* ^{36}Ar run with ^{36}Ar primary beams.

** ^{36}Ar run with ^{40}Ar primary beams.

Table 3

Effective RMS radii for Ar and Cl isotopes. R_{rms}^{m} are the effective RMS matter radii deduced by Glauber-model calculations in the optical-limit approximation, where we assume Fermi-type density distributions (Eq. (2)). R_{rms}^{p} are the effective RMS proton radii, deduced from optical isotope shift measurements [9], where we normalized the ^{36}Ar radius to that deduced from electron scattering [19]. R_{rms}^{n} are the effective RMS neutron radii, deduced by Eq. (3). ΔR are proton skin thicknesses, defined by (R_{rms}^{p} - R_{rms}^{n}).

Nucleus	R_{rms}^{m}	R_{rms}^{p}	R_{rms}^{n}	ΔR
	(fm)	(fm)	(fm)	(fm)
^{31}Ar	3.207±0.091			
^{32}Ar	3.075±0.089	3.228±0.018	2.866±0.220	0.362±0.221
^{33}Ar	3.090±0.086	3.225±0.017	2.920±0.201	0.305±0.202
^{34}Ar	3.142±0.037	3.203±0.017	3.071±0.084	0.132±0.086
^{35}Ar	3.157±0.040	3.202±0.017	3.109±0.086	0.093±0.087
^{36}Ar	3.184±0.035*	3.229±0.015	3.137±0.074	0.092±0.075
^{37}Ar	3.145±0.037	3.229±0.016	3.062±0.077	0.167±0.078
^{38}Ar	3.179±0.036	3.242±0.015	3.120±0.070	0.122±0.072
^{39}Ar	3.252±0.035	3.248±0.017	3.255±0.067	-0.007±0.069
^{40}Ar	3.282±0.036	3.257±0.016	3.301±0.065	-0.044±0.067
^{31}Cl	3.016±0.143			
^{32}Cl	3.045±0.153			
^{33}Cl	2.979±0.093			
^{34}Cl	3.084±0.076			
^{35}Cl	3.045±0.037			
^{36}Cl	3.128±0.038			
^{37}Cl	3.133±0.037			

* We used only the data with ^{36}Ar primary beams.

Figure captions

Fig. 1.
Schematic view of the experimental setup at the fragment separator FRS. TPC and MUSIC mean Time-Projection Chambers and Multi-Sampling Ion-Chamber, respectively. The bold letters indicate the measured quantities: TOF, $B\rho$ and ΔE.

Fig. 2.
Typical scatter plot of the mass-to-charge ratio (A/Z) versus the proton number (Z) at the FRS intermediate focus (F2) and the final focus (F4), for the ^{33}Ar nominal setting. ^{31}Cl fragments are also visible.

Fig. 3.
Doppler-corrected γ-ray energy spectra in a ^{12}C(^{34}Cl,^{34}Cl)X reaction at ~950 A MeV. The solid, long-dashed and short-dashed lines correspond to simulated spectra with 10, 20 and 40 mb of inelastic cross-sections. An exponential background, shown by the thin dashed line, was taken into account in the simulations.

Fig. 4.
Interaction cross-sections (σ_I) for (a) Ar and (b) Cl isotopes on carbon targets. The filled circles (squares) are data points obtained by runs with ^{36}Ar (^{40}Ar) primary beam, respectively. The solid line shows σ_I as calculated by Eq. (1).

Fig. 5.
Root-mean-square (RMS) matter radii (R_{rms}^{m}) for Ar and Cl isotopes. The solid lines show radii calculated by RMF calculations with the NL3 parameter set [20].

Fig. 6.
Isospin (T_z) dependence of RMS matter radii (R_{rms}^{m}) for A=31 systems. The closed (open) circles are radii deduced from the present (previous [2,3]) study. The solid lines show radii calculated by RMF calculations with NL3 parameterization [20]. The mirror pair ^{31}Ar-^{31}Al is marked by the dashed lines with arrows.

Fig. 7.
Mass number dependence of proton skin thickness in Ar isotopes. The solid lines connects radii calculated by RMF calculations with NL3 parameterization [20].

Fig. 8.

Correlation of the proton skin thickness as a function of the difference between the proton and neutron separation energy difference (S_p-S_n). The closed (open) circles marked with mass numbers are data for Ar (Na) isotopes, respectively. The cross marks show the calculated values from RMF calculations with the NL3 parameter set [20]; (×) for Ar isotopes and (+) for Na isotopes, respectively.

Fig. 1

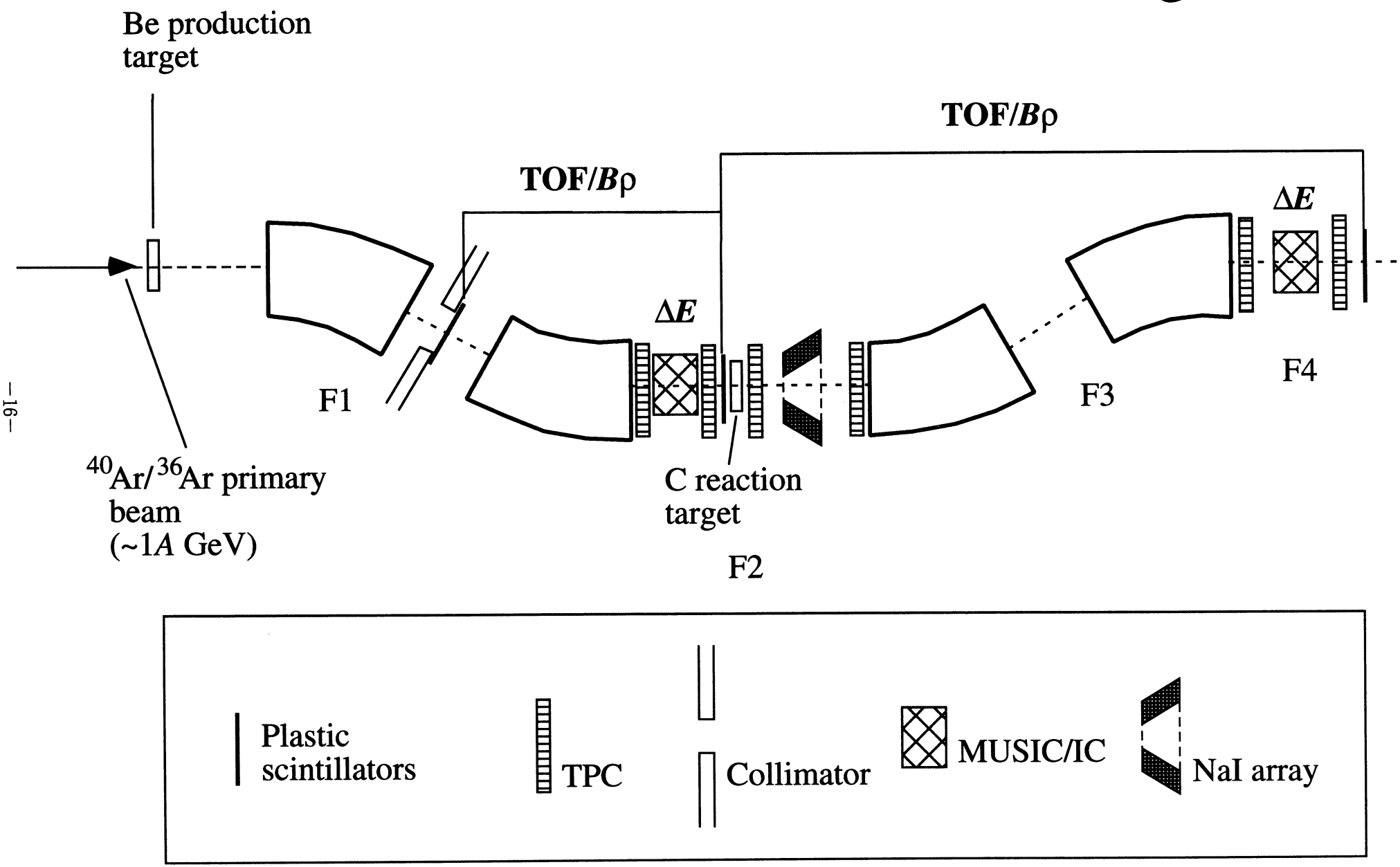
Be production target
TOF/Bρ
TOF/Bρ
ΔE
ΔE
F1
F2
F3
F4
^{40}Ar/^{36}Ar primary beam (~1A GeV)
C reaction target
Plastic scintillators
TPC
Collimator
MUSIC/IC
NaI array

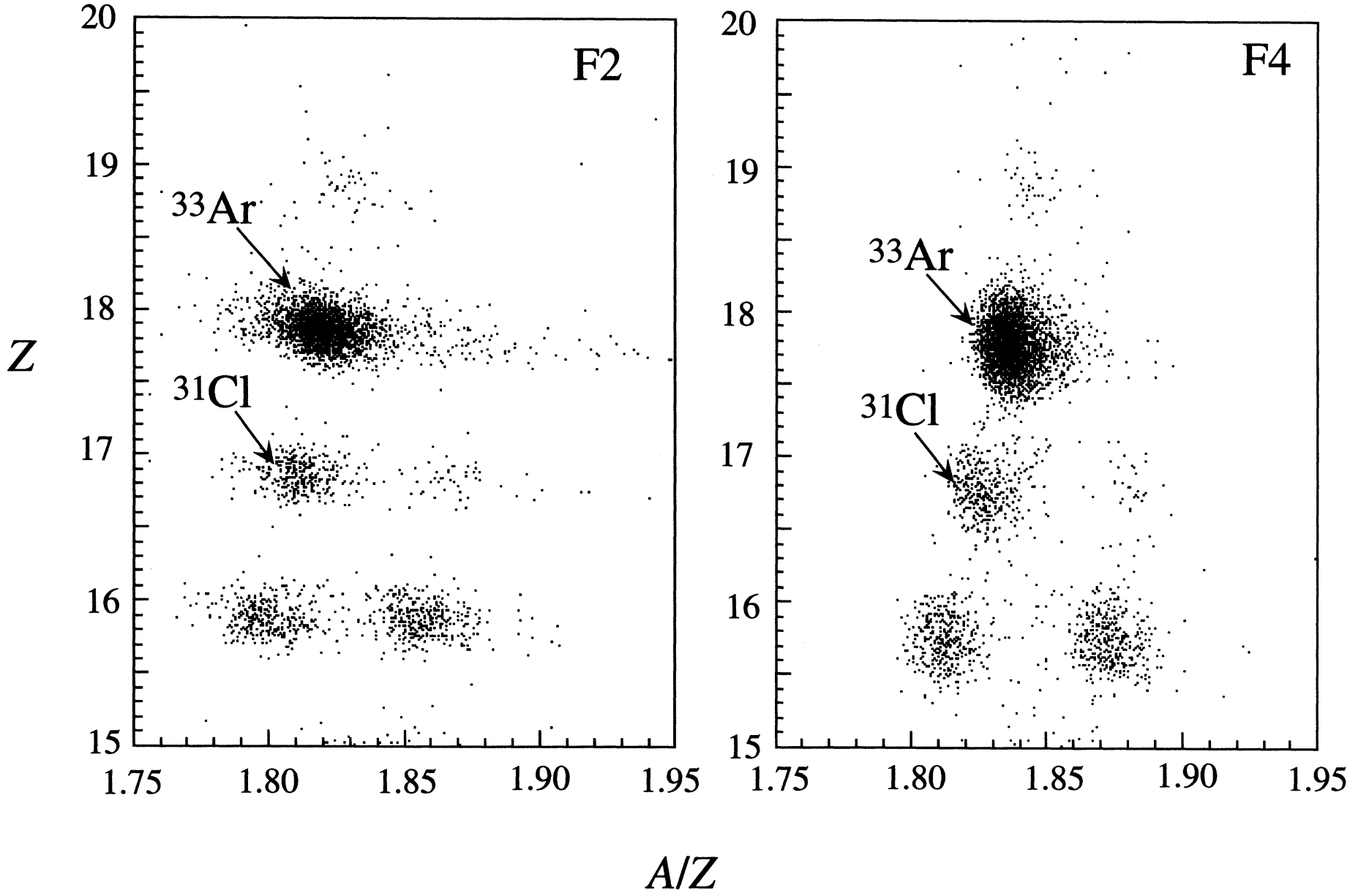
F2
F4
33Ar
31Cl
33Ar
31Cl
Z
A/Z
20
19
18
17
16
15
1.75
1.80
1.85
1.90
1.95

Fig.2

Fig. 3

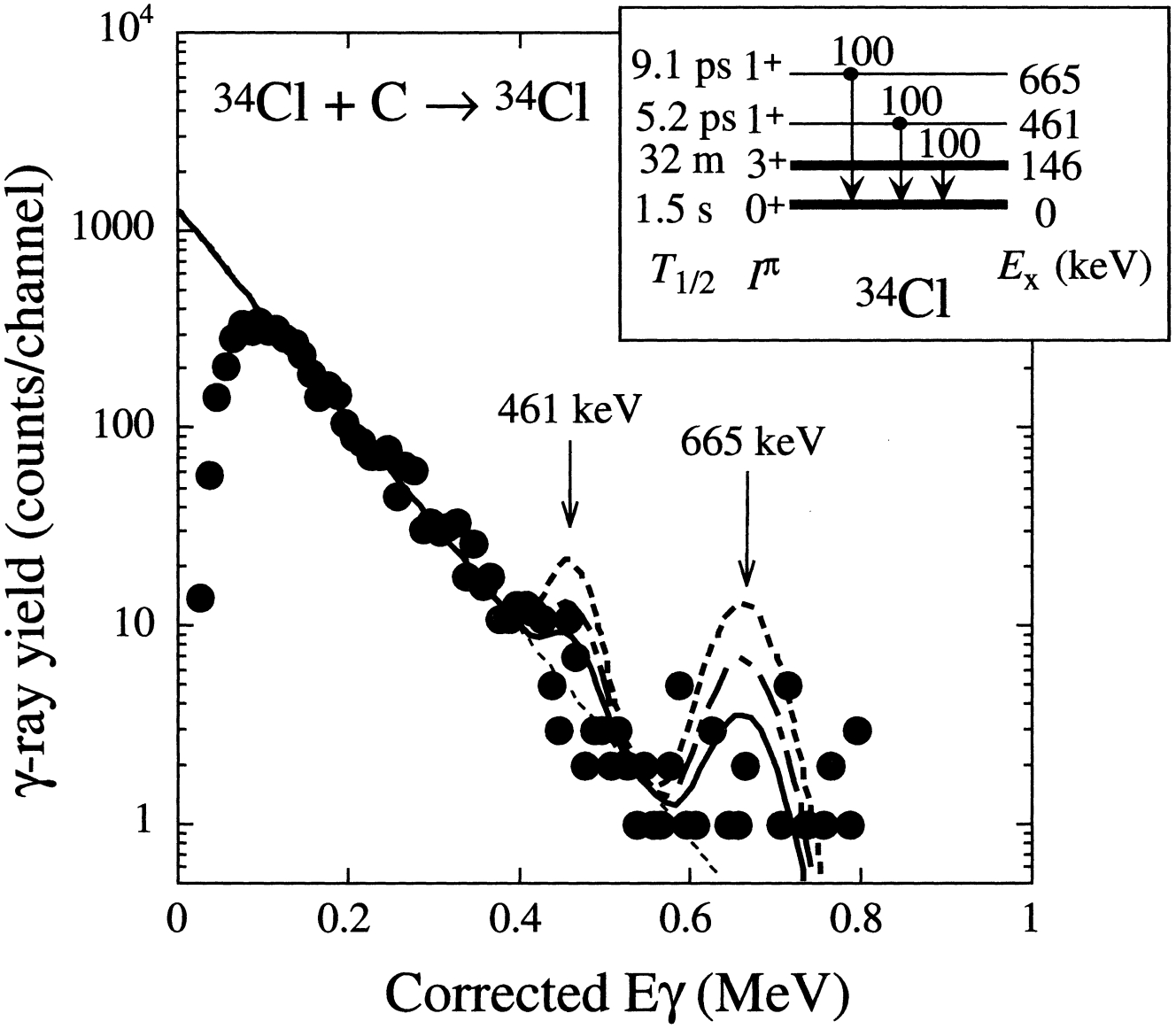
$^{34}Cl + C \rightarrow {}^{34}Cl$
9.1 ps 1+
5.2 ps 1+
32 m 3+
1.5 s 0+
100
100
100
665
461
146
0
$T_{1/2}$ I^{π}
^{34}Cl
E_x (keV)
461 keV
665 keV
γ-ray yield (counts/channel)
Corrected Eγ (MeV)
10^4
1000
100
10
1
0
0.2
0.4
0.6
0.8
1

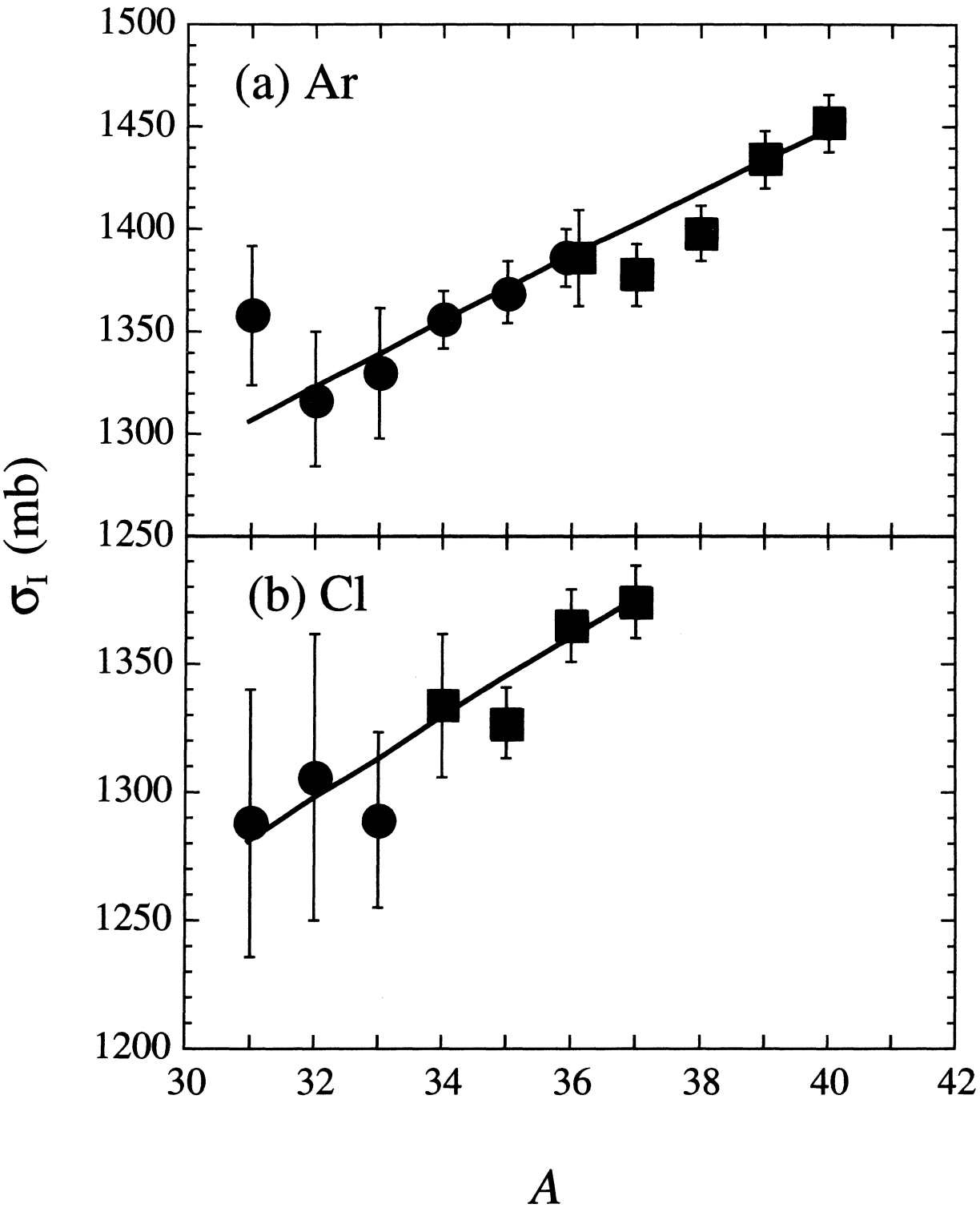
(a) Ar
(b) Cl
σ_I (mb)
1500
1450
1400
1350
1300
1250
1350
1300
1250
1200
30
32
34
36
38
40
42
A

Fig. 4

Fig. 5

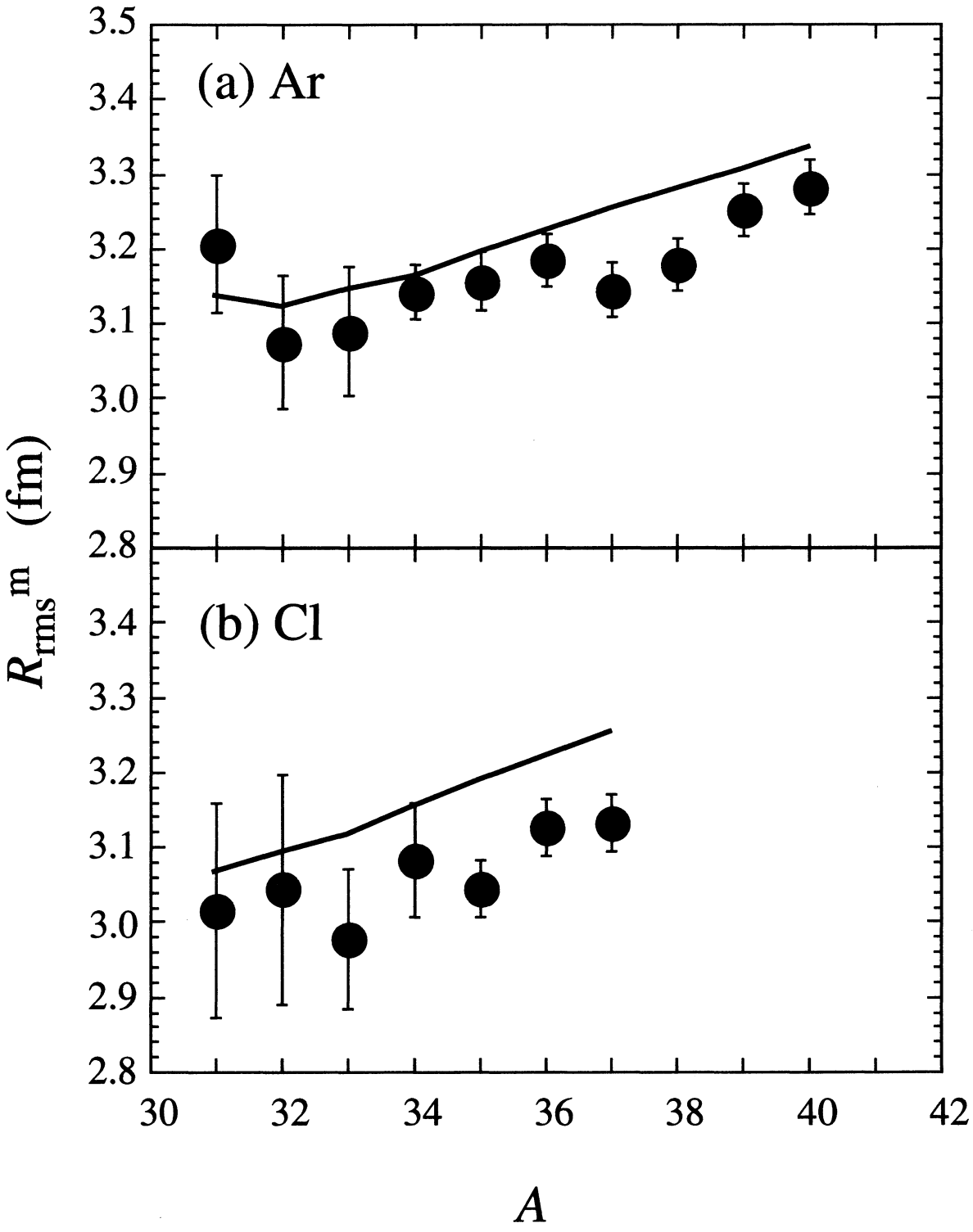

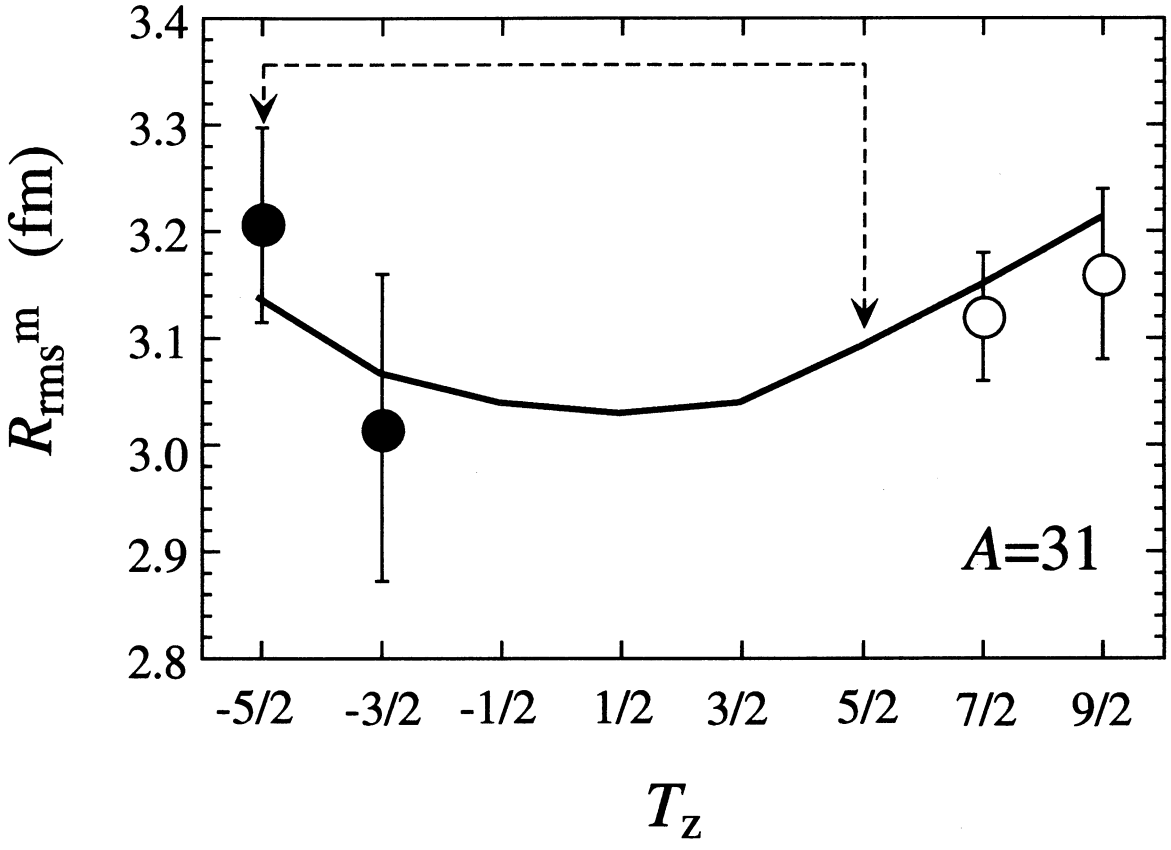

Fig.6

Fig. 7

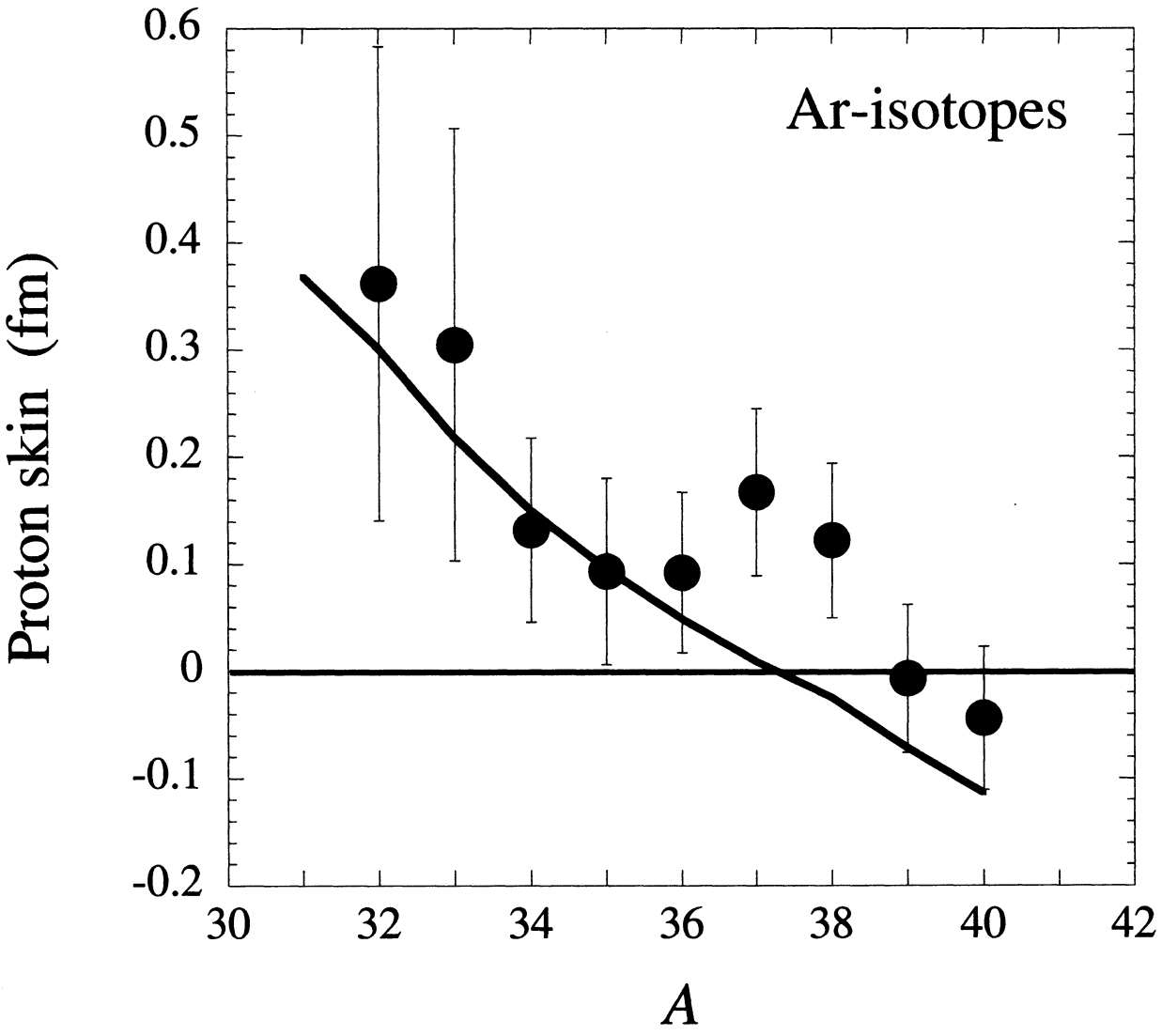
Ar-isotopes
Proton skin (fm)
0.6
0.5
0.4
0.3
0.2
0.1
0
-0.1
-0.2
30
32
34
36
38
40
42
A

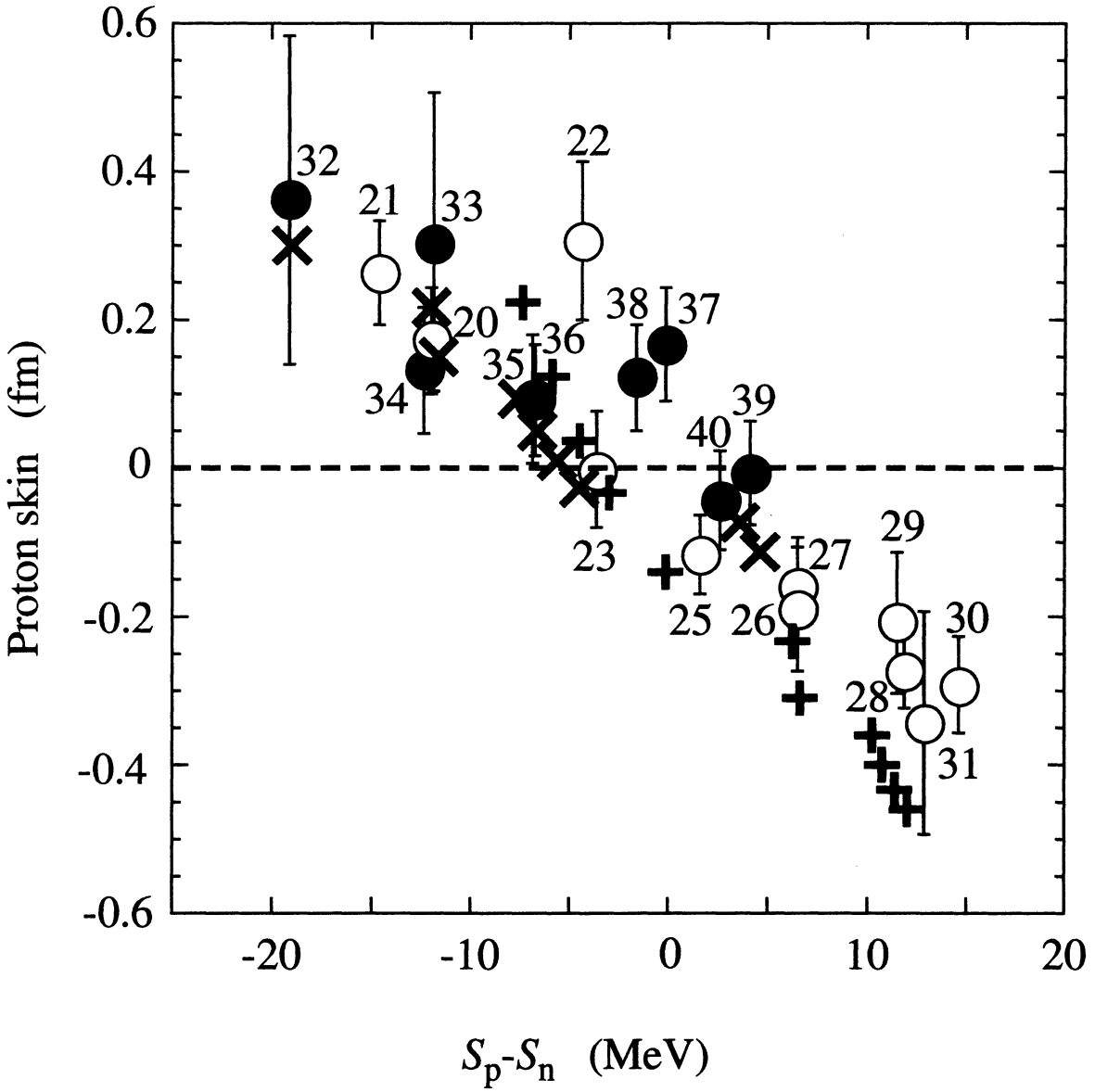
0.6
0.4
0.2
0
-0.2
-0.4
-0.6
-20
-10
0
10
20
Proton skin (fm)
S_p-S_n (MeV)
32
21
33
22
20
38
37
36
35
34
39
40
23
27
29
25
26
30
28
31

Fig. 8